Astron. Astrophys. 362, 1109–1121 (2000)

ASTRONOMY AND ASTROPHYSICS

# CO mapping and multi-line-analysis of Cepheus B

**H. Beuther[1,2], C. Kramer[2], B. Deiss[2,3], and J. Stutzki[2]**

[1] Max-Planck-Institut für Radioastronomie, Auf dem Hügel 69, 53121 Bonn, Germany
[2] I. Physikalisches Institut der Universität zu Köln, Zülpicher Strasse 77, 50937 Köln, Germany
[3] Physikalischer Verein, Robert Mayer Str.2–4, 60054 Frankfurt am Main, Germany

Received 24 July 2000 / Accepted 29 August 2000

**Abstract.** We present large scale (approx. $15\times15$ arcmin) on-the-fly maps of the Cepheus B molecular cloud in the $J$=3–2 and 2–1 transitions of $^{12}$CO, $^{13}$CO and C$^{18}$O obtained with the KOSMA 3m-telescope. We use these maps to study the spatial variation of the excitation conditions of the molecular gas. Additional CI observations allow to refine our analysis.

The gas temperature is dominated by UV radiation from identified adjacent and embedded sources plus additional heating by a hot core in the north-west of the cloud. A spherical clump PDR model allows to reproduce the observed line ratios at most positions. Only $^{12}$CO line ratios at the hot core position are inconsistent with this scenario and hence give evidence for additional heating mechanisms. Local volume densities are $\sim 2\cdot10^4$ cm$^{-3}$ while the average volume density of Cepheus B is less than $10^3$ cm$^{-3}$; thus, Cepheus B is highly clumped and the volume of these clumps fills only 2% to 4% of the whole cloud. Deep penetration of FUV radiation into the clumpy medium is consistent with the detection of [CI] emission from within the cloud. Abundance ratios of atomic carbon to CO are $\geq 0.2$.

The $^{13}$CO/C$^{18}$O integrated line intensity ratio rises significantly above the isotopic element ratio at the cloud edges where C$^{18}$O intensities are low. Possible explanations for this common observation in terms of fractionation and selective photodissociation on clump surfaces in a clumpy cloud are discussed.

**Key words:** molecular processes – stars: formation – ISM: clouds – ISM: molecules – ISM: structure – radio lines: ISM

## 1. Introduction

The molecular cloud Cepheus B, at a distance of 730 pc (Blaauw 1964), can be regarded as a typical example of sequential star formation. For a comprehensive review of earlier observations see Testi et al. (1995). Located at the edge of the HII region S155 and the Cepheus OB3 association, it comprises a compact HII region/hot core near the S155 interface, where young stars have already started to form (Moreno-Corral et al. 1993), and one might suspect that the process of star formation continues further inside the cloud. Cepheus B is an ideal target to investigate the spatial variations of excitation conditions, starting at a site of recent star formation and extending far into quiet parts of the cloud (see Fig. 1).

First large scale observations of the molecular material in the whole Cepheus region were conducted by Sargent et al. (1977) with the strongest $^{12}$CO 1–0 detection in Cepheus B. Later Minchin et al. (1992) observed the region around the previously detected compact HII region (Felli et al. 1978; in the following we refer to this region as the hot core) in $^{12}$CO 3–2 with a spatial resolution of $15''$ and found kinetic temperatures as high as 60 K.

Testi et al. (1995) resolved the hot core at 8.4 GHz and 14.9 GHz with VLA continuum observations into 4 substructures: one compact blister type HII region (heated probably by a B1 ZAMS star), confirming former predictions by Minchin et al. (1992), two pre-main-sequence stars and one smaller ionization front. Furthermore they detected a small cluster of young stars visible in the NIR and associated with the hot core. However, no other signposts of star formation like water masers or outflows were found in Cepheus B (Hughes 1988).

Olmi & Felli (1998) observed CS to study the dense gas in the immediate vicinity of the hot core and detected weaker CS emission than observed in other massive star forming regions (Cesaroni et al. 1999). They find that the hot core is in an advanced state of star forming activity where new stars have destroyed the molecular material and thus reduced the column densities.

Most of the recent investigations concentrated on the Cepheus B hot core and its immediate surroundings. In contrast to this, the observations presented here deal with structures of Cepheus B on larger scales. Our main interest is the variation of excitation conditions of the molecular material from the hot core to inner regions of the cold molecular cloud.

The outline of this paper is as follows: Sect. 2 gives a description of the observations, Sect. 3 presents the observational results, in Sect. 4 a multi-line-analysis of the data set is conducted, Sect. 5 discusses our results and Sect. 6 summarizes the output of our analysis.

## 2. Observations

The observations of Cepheus B were carried out with the 3m KOSMA submillimeter telescope at Gornergrat, Switzerland

*Send offprint requests to*: H. Beuther (beuther@mpifr-bonn.mpg.de)

**Table 1.** Observing parameters: line frequency, beam efficiency $B_{\rm eff}$, beam width, observing mode, grid spacing, number of observed positions, mean atmospheric zenith opacity $\langle\tau_{\rm atm}\rangle$, rms of spectra $\langle T_{\rm mb}^{\rm rms}\rangle$, channel width $\Delta v_{\rm ch}$, and observing period

| transition | frequency [GHz] | $B_{\rm eff}$ [%] | HPBW [$''$] | mode | grid [$''$] | pos. | $\langle\tau_{\rm atm}\rangle$ | $\langle T_{\rm mb}^{\rm rms}\rangle$ [K] | $\Delta v_{\rm ch}$ [km s$^{-1}$] | Observing period |
|---|---|---|---|---|---|---|---|---|---|---|
| $^{12}$CO 2–1 | 230.538 | 68 | 120 | OTF | 30 | 1120 | 0.39 | 2.0 | 0.21 | October 98 |
| $^{13}$CO | 220.399 | 68 | 120 | OTF | 30 | 1080 | 0.21 | 0.73 | 0.22 | October 98 |
| C$^{18}$O | 219.560 | 68 | 120 | OTF | 30 | 756 | 0.015 | 0.21 | 0.22 | October 98 |
| $^{12}$CO 3–2 | 345.796 | 55 | 80 | OTF | 30 | 1080 | 0.89 | 1.33 | 0.29 | October 98 |
| $^{13}$CO | 330.59 | 55 | 80 | OTF | 30 | 624 | 0.37 | 0.8 | 0.30 | October 98 |
| C$^{18}$O | 329.330 | 73 | 80 | OTF | 30 | 264 | 0.54 | 0.57 | 0.24 | March 99 |
| CI $^3P_1$–$^3P_0$ | 492.161 | 60 | 50 | PSw | – | 2 | 1.6 | 0.25 | 0.42 | March 98 |

(Winnewisser et al. 1986, 1990; Kramer et al. 1998, 2000). On-the-fly maps of the 2–1 and 3–2 low-$J$ transitions of CO and its isotopomers $^{12}$CO, $^{13}$CO, and C$^{18}$O were conducted in 5 nights between October 14 and 21 1998, the C$^{18}$O 3–2 data were taken in 3 nights in March 1999. We used the Cologne dual-channel 230/345 GHz SIS receiver (Graf et al. 1998), which has tunerless waveguide mixers (Haas et al. 1997) and is mounted at one of the two Nasmyth ports. DSB receiver noise temperatures were about 120 K. As backends we used the Cologne medium and variable resolution acousto optical spectrometer (Schieder et al. 1989) with bandwidths of 1 GHz and a channel spacing of 160 kHz (330 kHz) at 230 (345) GHz. The observational parameters are summarized in Table 1.

All data were taken in a newly implemented, efficient on-the-fly (OTF) observing mode, the details of which are discussed in Appendix A. After observing the OFF-position and after moving to the source, the telescope keeps moving in right-ascension or in declination at a constant speed across the source while taking data at a constant rate. For the data presented here, we decided to restrict the total time for such OFF-ON-cycles to 2.5–3 minutes. The ON-data were integrated over 4 sec each in spatial steps of $30''$, corresponding to Nyquist sampling the KOSMA 3m-telescope beam at the highest observing frequency, 345 GHz. The source was covered 5 to 10 times and single fields were combined to cover the total area. First order (in a few cases second order) baselines were subtracted from the data. All data analysis was done using the GILDAS package of IRAM and the Observatoire de Grenoble.

In addition, we observed the [CI] $^3P_1$–$^3P_0$ transition at two positions in position switching mode (PSW, Table 1). A dual-channel receiver working at 492/810 GHz (Stutzki et al. 1997) was used to observe the lower [CI] transition, SSB receiver temperature at 492 GHz were $\sim 160$ K. The higher receiver and system temperature at 810 GHz did not allow to detect the $^3P_2$–$^3P_1$ transition. The variable resolution AOS was used with 685 kHz channel spacing (Table 1). The CI spectra suffered partly from baseline ripples, we therefore subtracted fifth order baselines from the original spectra.

Measurements on Jupiter were deconvolved to derive the HPBW of the antenna pattern (Table 1); main beam efficiencies $B_{\rm eff}$ were derived using disk brightness temperatures compiled by Griffin et al. (1986). The forward efficiency $F_{\rm eff}$ derived from skydips is 90%.

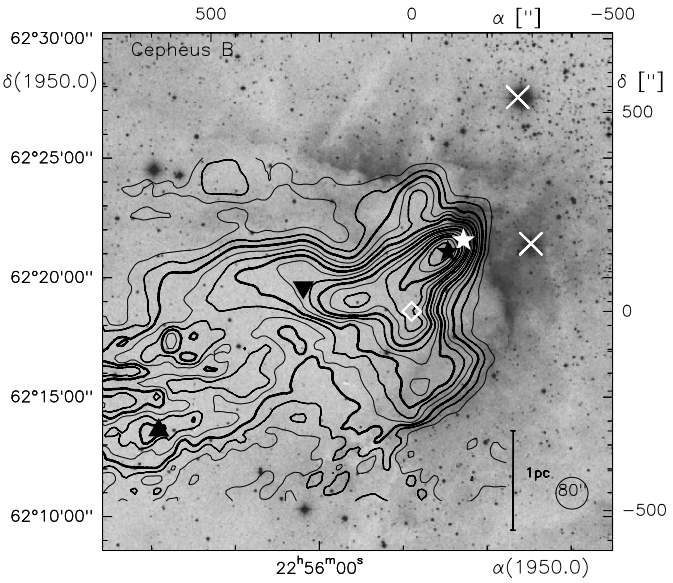


**Fig. 1.** Velocity integrated $^{12}$CO 3–2 intensities in contours overlayed on an optical picture (red POSS plate) of Cepheus B and the HII region S155. The range of integration is $-18$ to $-8$ km s$^{-1}$. Contour levels are 4 by 6 to 94 K km s$^{-1}$. The white crosses indicate the O7 star HD217086 (north-west) and the B1 star HD217061; the white $\star$ denotes the hot core region. In addition, we marked, as reference for the further analysis, the positions of strongest $^{12}$CO, $^{13}$CO, and C$^{18}$O peak temperatures by a $\star$, a $\diamond$ and a filled $\bigtriangledown$; a fourth position in the south western part is marked by a filled $\bigtriangleup$.

The sky transmission was estimated by measuring the radiation temperature of the blank sky at the elevation of the astronomical source. Analogous to the standard chopper wheel calibration, we then corrected the intensities to the antenna temperature ($T_A^*$) scale. The $^{13}$CO 3–2 data at 330 GHz and the CI line at 492 GHz were corrected for atmospheric sideband imbalance derived from standard atmospheric models (Grossman 1989).

Line intensities presented in this paper are on the main beam temperature scale, $T_{\rm mb} = (F_{\rm eff}/B_{\rm eff})T_A^*$ (Downes 1989). $^{12}$CO 3–2 and $^{13}$CO 3–2 data of summer 1998 are corrected for the influence of an underlying error beam (Eqs. B.1, B.2, B) due to a poorer surface accuracy at this period, which affected the 345 GHz efficiencies far more than the 230 GHz efficiencies. The calibration accuracy is estimated to about 15%.

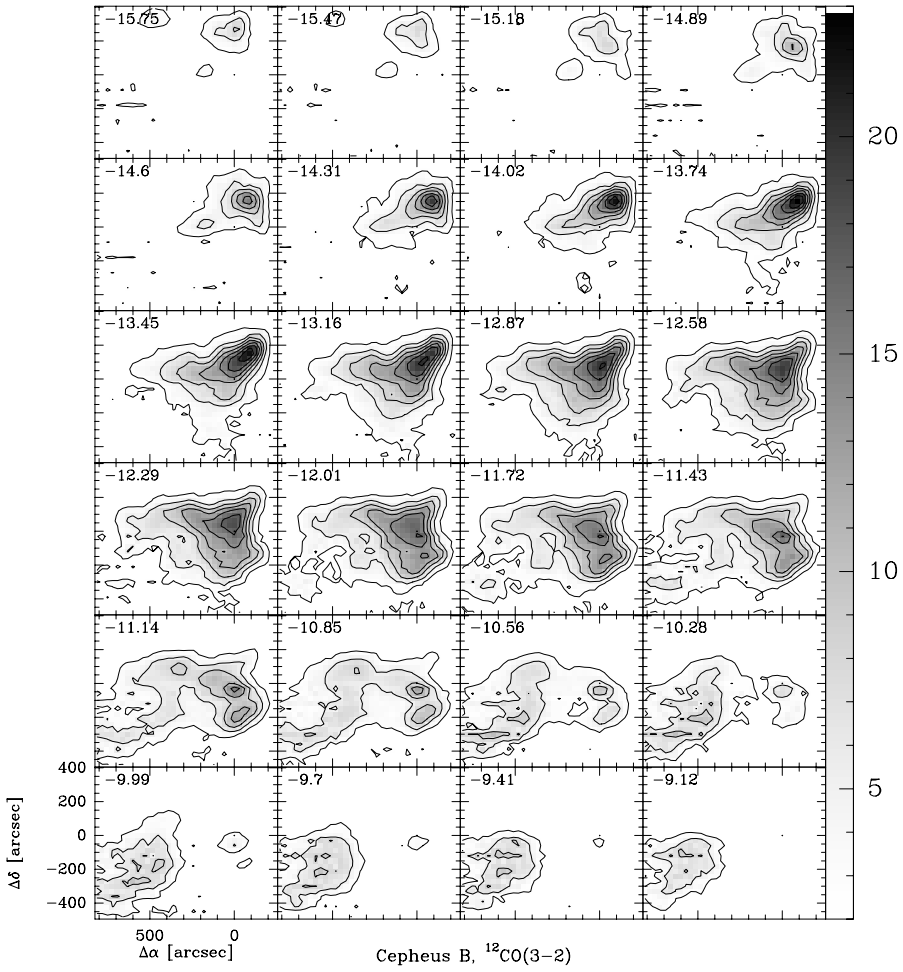


**Fig. 2.** Channel map of the $^{12}$CO 3–2 emission. The velocity varies from $-15.75\,\mathrm{km\,s^{-1}}$ to $-9.12\,\mathrm{km\,s^{-1}}$, the channel width is $0.28\,\mathrm{km\,s^{-1}}$, and the contours are 2 by 3 to 23 $\mathrm{Kkm\,s^{-1}}$.

The (0,0) position of our maps is $\alpha(1950) = 22^{\mathrm{h}}55^{\mathrm{m}}27\overset{\mathrm{s}}{.}0$, $\delta(1950) = 62^{\circ}18'37\overset{''}{.}0$. The OFF-position lies $10'$ to the west and was checked to be free of CO emission. An optical pointing camera, mounted parallel to the radio axis of the telescope, is used during weekly pointing sessions to derive new telescope pointing constants and to correct for local pointing offsets. During day time, radio pointing was checked on Jupiter. The pointing accuracy was better than $20''$.

## 3. Observational results

### *3.1.* $^{12}$CO *3–2 data*

The $^{12}$CO 3–2 observations enclose an area of 4 pc×3.5 pc ($17.5' \times 14'$) (Fig. 1). The molecular cloud is bound by the HII region S155 in the north-west, a large arc-shaped optical emission region, and it has a linear extent of $\geq 5$ pc in south-eastern direction. The CO emission peaks near the hot core region and decreases towards the south-east, showing only rather weak substructures at this resolution.

In the channel maps, however, small scale structure is much more pronounced (Fig. 2). The north-western part of the cloud near the hot core emits at $-15\,\mathrm{km\,s^{-1}}$, which confirms its association with S155 having the same system velocity (Miller 1968, derived from $H_\alpha$ observations) while the south-eastern part emits at $-10\,\mathrm{km\,s^{-1}}$. Near $-14\,\mathrm{km\,s^{-1}}$ the cloud looks like a compact cometary globule pointing towards S155. With increasing velocity the emission region extends further south-east. The cloud appears filamentary at around $-10.9\,\mathrm{km\,s^{-1}}$. At $-9.7\,\mathrm{km\,s^{-1}}$ the cloud again looks compact in the south-east near ($600''/-200''$). Slight indications of scanning artefacts are visible in the south-eastern part of the maps.

The observed spectra show close to Gaussian line shapes (Fig. 3); neither line wings nor self absorption features due to cold foreground material show up prominently. Only a few spectra show shoulders, probably due to more than one velocity component; the average line width (FWHM) is $2.8\,\mathrm{km\,s^{-1}}$ and varies marginally throughout the cloud. Fig. 3 shows spectra at the four representative positions marked in Fig. 1.

### *3.2. Further CO data*

We also conducted OTF mapping in $^{12}$CO 2–1, $^{13}$CO 3–2 and 2–1, and $C^{18}O$ 3–2 and 2–1 (Fig. 4; note: the $^{13}$CO 3–2 and $C^{18}O$ 3–2, 2–1 maps are spatially less extended). Each transition samples different regimes of temperatures and densities, described e.g. by its critical density needed for thermalization and its energy of the upper level above the ground state (Table 2).

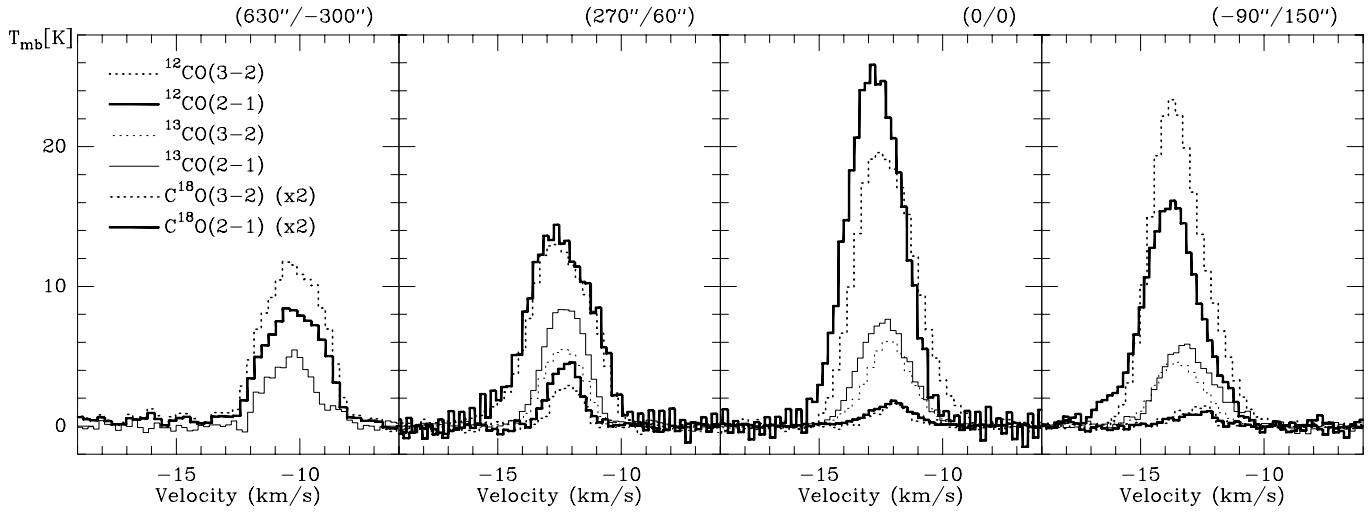


**Fig. 3.** Spectra of the different transitions measured in Cepheus B at the 4 positions selected for the radiation transfer analysis (marked in Fig. 1). All spectra are smoothed to a spatial resolution of $120''$; the $^{12}$CO 3–2 and $^{13}$CO 3–2 spectra are error beam corrected (Appendix B). (The additional noise, seen in the two $^{12}$CO 2–1 spectra at $(270''/60'')$ and $(0''/0'')$, was caused by a temporal technical even-odd problem of the AOS, which is now solved.)

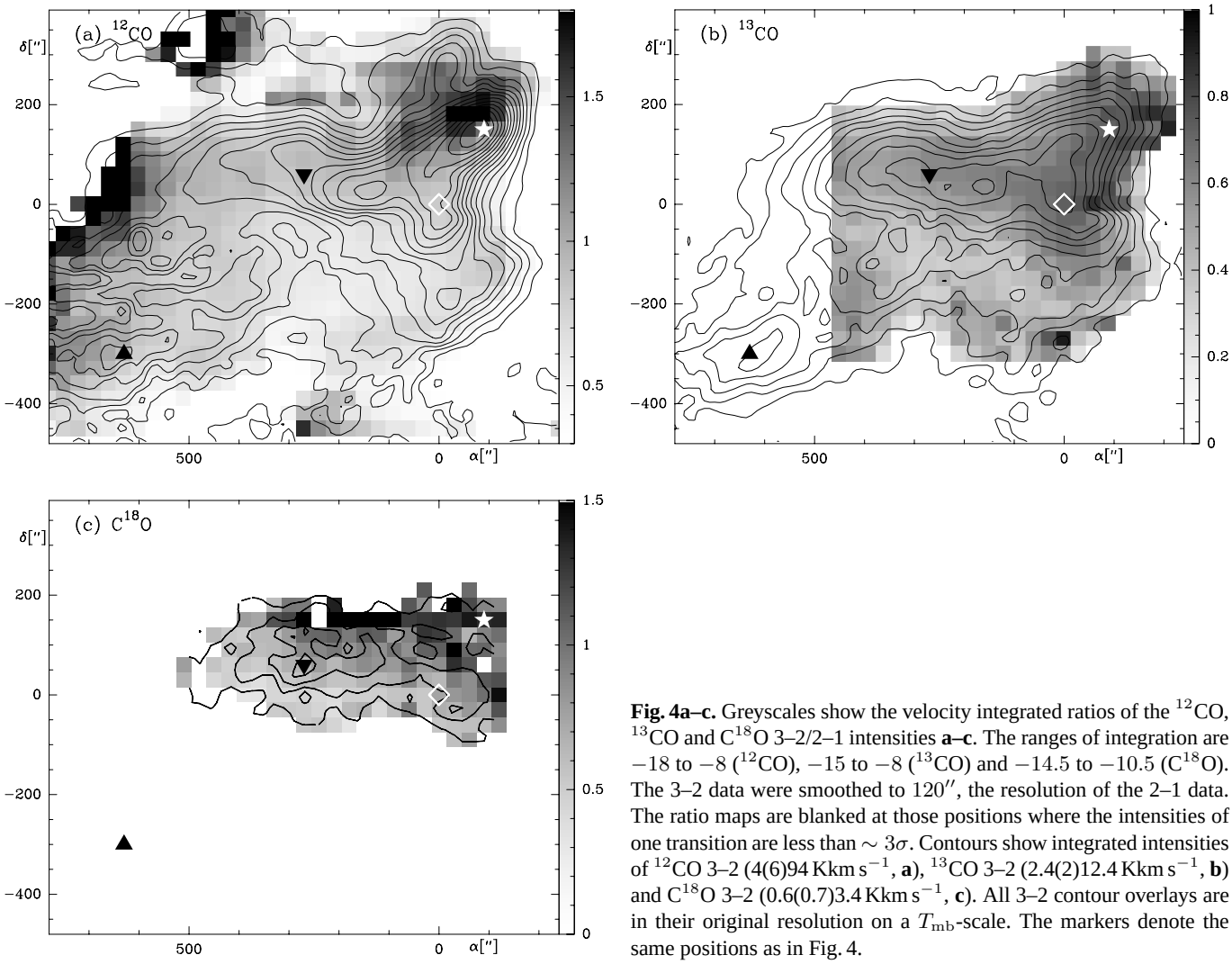


**Fig. 4a–c.** Greyscales show the velocity integrated ratios of the $^{12}$CO, $^{13}$CO and C$^{18}$O 3–2/2–1 intensities **a–c**. The ranges of integration are $-18$ to $-8$ ($^{12}$CO), $-15$ to $-8$ ($^{13}$CO) and $-14.5$ to $-10.5$ (C$^{18}$O). The 3–2 data were smoothed to $120''$, the resolution of the 2–1 data. The ratio maps are blanked at those positions where the intensities of one transition are less than $\sim 3\sigma$. Contours show integrated intensities of $^{12}$CO 3–2 (4(6)94 Kkm s$^{-1}$, **a**), $^{13}$CO 3–2 (2.4(2)12.4 Kkm s$^{-1}$, **b**) and C$^{18}$O 3–2 (0.6(0.7)3.4 Kkm s$^{-1}$, **c**). All 3–2 contour overlays are in their original resolution on a $T_{\rm mb}$-scale. The markers denote the same positions as in Fig. 4.

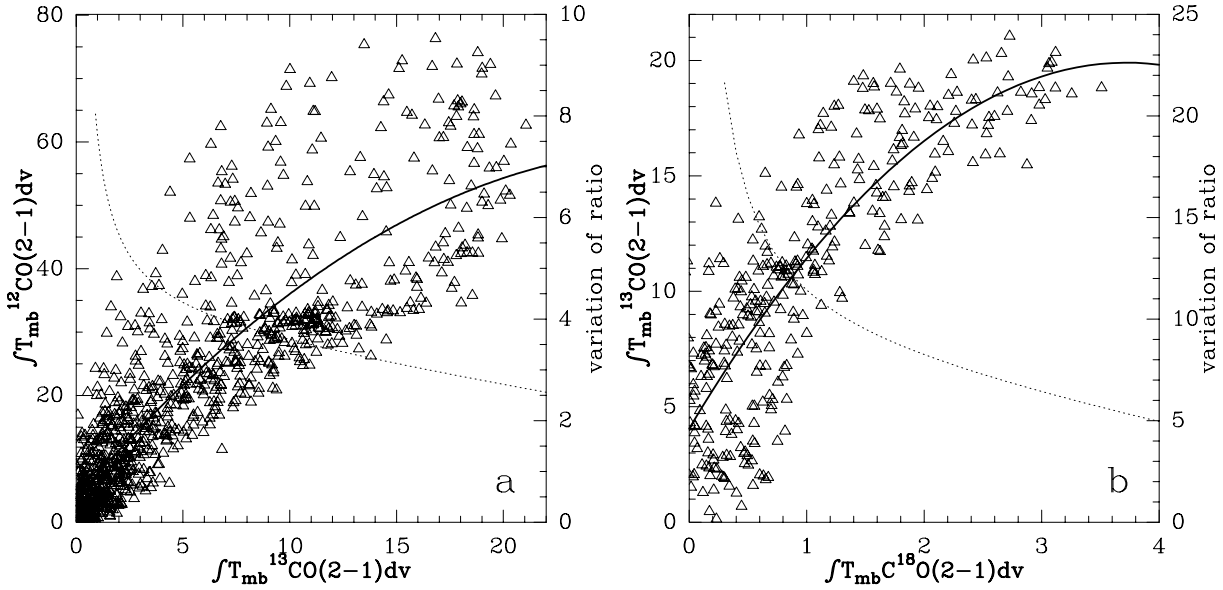


**Fig. 5.** **a** Integrated intensity of $I_{mb}(^{12}\mathrm{CO}$ 2–1) against $I_{mb}(^{13}\mathrm{CO}$ 2–1), the solid line shows the best fit of a 2. order polynomial. The dashed line shows the intensity ratio derived from the fit for integrated intensities larger than $1\sigma$ (2.9 Kkm s$^{-1}$ for $I_{mb}(^{12}\mathrm{CO}$ 2–1) and 0.9 Kkm s$^{-1}$ for $I_{mb}(^{13}\mathrm{CO}$ 2–1)). **b** The same for $^{13}$CO and C$^{18}$O ($1\sigma$ for $I_{\mathrm{mb}}$(C$^{18}$O 2–1) equals 0.2 Kkm s$^{-1}$).

The distribution of velocity integrated brightness temperatures ($I_{mb} = \int T_{mb}\ dv$) naturally differs between the different isotopomers (contour maps in Fig. 4), given the isotopomeric abundance ratios ([$^{12}$CO]/[H$_2$]=$8.5 \cdot 10^{-5}$, Frerking et al. 1982; [$^{12}$CO]/[$^{13}$CO]=67, Langer & Penzias 1990; and [$^{12}$CO]/[C$^{18}$O]=470, Frerking et al. 1982), and hence optical depth differences between the various lines. The $^{13}$CO 3–2 map peaks near the $(0''/0'')$ position (the position of strongest CO 1–0 emission, Sargent et al. 1977) at a distance of 0.7 pc to the hot core, and the C$^{18}$O map peaks still further east at $(270''/60'')$ at a projected distance of 1.7 pc. Both rarer species show an east-west oriented ridge of emission at $\sim \Delta\delta = 50''$. The map of $^{13}$CO shows another ridge of emission extending from the peak of C$^{18}$O emission in south-eastern direction. Thus, the general tendency is that the rarer the isotopomers, the more does their emission peak towards the projected central position of the cloud and away from the HII region/molecular cloud interface. The spatial variation in integrated line intensities, e.g. at a scale of 0.5 pc perpendicular to the east-west orientated ridge, is much stronger in C$^{18}$O than in $^{13}$CO, which in turn shows a higher contrast than $^{12}$CO. The hot core region is not pronounced in the rarer isotopomers.

From the distribution of integrated intensity ratios 3–2/2–1 (greyscale maps in Fig. 4) one can distinguish at least three regions: the interface region to S155 near the hot core showing high line ratios of 1.5 to 2 in $^{12}$CO and slightly lower in the other isotopomers; the bulk of the cloud, characterized by ratios of about 1 in all isotopomers and orientated along the east-west ridge; the north-eastern edge of the $^{12}$CO map exhibiting similarly high $^{12}$CO 3–2/2–1 line ratios as the hot core region, although with lower integrated intensities. The integrated intensity ratios

**Table 2.** Parameters of the observed transitions; ref.: Lovas 1988, Flower & Launay 1985, Schröder et al. 1991.

| | | h$\nu$/k [K] | $E_{\mathrm{u}}$/k [K] | $n_{\mathrm{cr}}$ [cm$^{-3}$] |
|---|---|---|---|---|
| $^{12}$CO | $2-1$ | 11.1 | 16.6 | $2 \cdot 10^4$ |
| | $3-2$ | 16.6 | 33.2 | $5 \cdot 10^4$ |
| CI | $^3\mathrm{P}_1 \rightarrow {}^3\mathrm{P}_0$ | 23.6 | 23.6 | $1 \cdot 10^3$ |

$$^{12,13}\mathcal{R}^I = I_{mb}(^{12}\mathrm{CO})/\mathrm{I_{mb}}(^{13}\mathrm{CO})$$
$$^{13,18}\mathcal{R}^I = I_{mb}(^{13}\mathrm{CO})/\mathrm{I_{mb}}(\mathrm{C}^{18}\mathrm{O})$$

are strongly correlated with the integrated intensities of $I_{mb}(^{13}\mathrm{CO})$ and $I_{mb}(\mathrm{C}^{18}\mathrm{O})$, respectively.

The $^{12,13}\mathcal{R}^I$ ratio (dashed curve in Fig. 5a) varies between $\sim 2.5$, for high values of $I_{mb}(^{13}\mathrm{CO})$, and more than 8 for low values of the integrated $^{13}$CO intensity (the interstellar abundance ratio is $\approx 67$). This variation and fluctuation is consistent with varying optical depths of the $^{13}$CO isotopomer and optically thick $^{12}$CO emission. Considering LTE with $\tau(^{12}\mathrm{CO}) >> 1$ the $^{13}$CO opacity, given by $\tau = -\ln(1-I_{mb}(^{13}\mathrm{CO})/I_{mb}(^{12}\mathrm{CO}))$, varies between 0.4 in the center of the cloud where intensities are high, and 0.03 at the cloud edges.

The integrated intensity ratio $^{13,18}\mathcal{R}^I$ (dashed curve in Fig. 5b), derived from the fit, variies between $\sim 5$ for high integrated C$^{18}$O intensities and more than 22 at the cloud edges where C$^{18}$O intensities and column densities are low. In contrast to the former plot, most positions show a $^{13,18}\mathcal{R}^I$ ratio that is higher than the abundance ratio which is 7 in this case. Clumpy cloud models, isotope-selective photodissociation and/or chemical fractionation are possible approaches to explain this common phenomenon. Sect. 5 will compare and discuss our findings with similar results from the literature.

**Table 3.** Measured ratios of line peak temperature at 4 Positions and their mean value. Estimated line calibration errors are 15%, ratio errors around 20%. The last two columns show the ratio–mean and the ratio–range of the integrated intensities over the whole mapped region. The high upper limits in the range-column are seen only at edges of the cloud.

| | ratios of peak line temperatures | | | | | ratios of integrated intensities | |
|---|---|---|---|---|---|---|---|
| | $(630''/-300'')$ | $(270''/60'')$ | $(0''/0'')$ | $(-90''/150'')$ | mean | mean | range |
| $^{12}$CO 3–2/2–1 | 0.8 | 1.0 | 0.8 | 1.5 | 1.0 | 0.8 | 0.7–3 |
| $^{13}$CO 3–2/2–1 | – | 0.6 | 0.8 | 0.8 | 0.7 | 0.5 | 0.3–0.9 |
| C$^{18}$O 3–2/2–1 | – | 0.7 | 0.9 | 1.3 | 1.0 | 0.8 | 0.5–1.8 |
| $^{12}$CO/$^{13}$CO 3–2 | – | 2.3 | 3.5 | 4.9 | 3.6 | 6.9 | 2–20 |
| $^{12}$CO/$^{13}$CO 2–1 | 2.1 | 1.6 | 3.4 | 2.7 | 2.5 | 3.8 | 2–11 |
| $^{12}$CO/C$^{18}$O 3–2 | – | 11 | 36 | 57 | 34.7 | 40.5 | 11–80 |
| $^{12}$CO/C$^{18}$O 2–1 | – | 6 | 32 | 39 | 25.7 | 28.5 | 6–55 |
| $^{13}$CO/C$^{18}$O 3–2 | – | 2.4 | 10 | 12 | 8.1 | 8.6 | 2.4–20 |
| $^{13}$CO/C$^{18}$O 2–1 | – | 4 | 9 | 14 | 9.0 | 9.2 | 4–15 |

## 4. Multi line analysis

With the aim to understand changes in excitation conditions of molecular material in a FUV illuminated cloud like Cepheus B we try to reproduce the observed data by several model calculations. Already rather simple LTE calculations and escape probability models set reasonably good constraints on the excitation conditions, and where these models fail they indicate the necessity for more sophisticated, and realistic modelling. As a further approach we therefore apply a PDR model, which provides a self-consistent treatment of the chemical and thermal balance of a cloud together with the radiative transfer of CO line emission in spherical clouds illuminated by an isotropic FUV field.

First, assuming LTE with a beam filling factor $F_b$ of 1 we derive an estimate of the average kinetic temperature, density and mass in Cepheus B. We averaged the $^{12}$CO 3–2 and C$^{18}$O 2–1 data seperately over the area of significant emission in C$^{18}$O 2–1 ($-180'' < \Delta\alpha < 420''$, $-120'' < \Delta\delta < 180''$, Fig. 4) and find from the optically thick $^{12}$CO a mean excitation temperature of 22 K. Using the C$^{18}$O data, this temperature, and the canonical [C$^{18}$O]/[H$_2$] abundance ratio, the derived average LTE H$_2$ column density per beam is $4 \cdot 10^{21}$ cm$^{-2}$ and the average H$_2$ volume density is $n_{\rm av}$ =860 cm$^{-3}$, assuming that the cloud is as extended along the line-of-sight as across the face of the cloud. The average $^{13}$CO optical depth is $\sim 0.4$ in this center region and C$^{18}$O is optically thin with opacities varying between 0.1 and 0.01. The total mass derived from C$^{18}$O 2–1 is 200 M$_\odot$. One should note that this is a rather accurate estimate, as the conversion from integrated C$^{18}$O intensity to H$_2$ column density is not strongly affected by the detailed excitation conditions, as long as the densities are above the critical density of the transition (e.g. Stutzki et al. 1993).

Since the above calculation only leads to the average density and does not take into account non-thermal excitation nor any difference in the kinetic temperatures of the $^{12}$CO and C$^{18}$O emitting regions, we used an escape probability radiative transfer model (Stutzki & Winnewisser 1985) as a next step. It assumes a homogeneous, spherical symmetric cloud with constant kinetic temperature and volume density. While it is clear that real clouds are still much more complicated, such a model is commonly used and its results improve on the simple LTE analysis. Especially, the derived densities and temperatures refer to localized values. Collision rates were taken from Flower & Launay (1985) and models were calculated for kinetic temperatures between $T_{kin}$ = 10–100 K, H$_2$ volume densities $0.5 \cdot 10^3 - 3 \cdot 10^5$ cm$^{-3}$ and CO column densities $0.5 \cdot 10^{14} - 1 \cdot 10^{19}$ cm$^{-2}$.

### *4.1. Results of the escape probability analysis*

We apply the model to interpret the spectral lines observed at four positions (Fig. 3), sampling different regions of Cepheus B. To circumvent the problem of varying beam filling factors, we try to find models which fit best the observed line ratios (Table 3). $^{12}$CO and $^{13}$CO 3–2/2–1 line ratios are susceptible to volume densities and temperatures, whereas the line ratios between different isotopomers respond to variations of column densities. Results of this analysis are summarized in Table 4.

#### 4.1.1. Volume densities

The ratio of $^{12}$CO 3–2/2–1 peak line temperatures lies between 0.8 and 1.5 at the four positions, indicating that these two transitions are thermalized. Indeed, the data are consistent with escape probability models of densities of about the critical density (Table 2) of a few $10^4$ cm$^{-3}$. This result is typical: depending on the molecule and transition observed, local densities derived from these lines are usually near their critical densities (e.g. Stutzki 1993). Local densities in Cepheus B are a factor of $\sim 10$ higher than the average density derived assuming LTE, another result which is commonly found, and which indicates that the emitting regions are not homogeneous but exhibit significant substructure.

**Table 4.** Results of the escape probability analysis of the peak line ratios (3–2/2–1) at the four selected positions: $H_2$ column densities, local $H_2$ volume densities and kinetic temperatures. See explanations in the text.

| Isot. | | $(630'', -300'')$ | $(270'', 60'')$ | $(0'', 0'')$ | $(-90'', 150'')$ |
|---|---|---|---|---|---|
| | $N(\mathrm{H_2})[10^{22}\mathrm{cm}^{-2}]$ | $> 2.6$ | $1.9 < x < 4.7$ | $0.4 < x < 1.2$ | $1.2 < x < 2.3$ |
| | $n_{\rm loc}(\mathrm{H_2})[10^{4}\mathrm{cm}^{-3}]$ | $< 2.5$ | $0.8 < x < 4.0$ | $1.0 < x < 4.0$ | $1.6 < x < 4.0$ |
| $^{12}$CO | $T_{\rm kin}$[K] | $> 20$ | $> 30$ | $> 30$ | $> 70$ |
| $^{13}$CO | $T_{\rm kin}$[K] | $> 20$ | $< 20$ | $> 30$ | $\sim$20 |
| C$^{18}$O | $T_{\rm kin}$[K] | – | $< 20$ | $> 30$ | $\sim$40 |

#### 4.1.2. Column densities

$H_2$ column densities, derived from line ratios and the escape probability models, vary between 0.4 and $5 \cdot 10^{22}$ cm$^{-2}$ at the four positions. They are larger by a factor of upto 10 than the average column density per beam derived from integrated C$^{18}$O intensities assuming LTE. This is a further indication of structure within the beam and low beam filling factors, as will be shown later. Subthermal excitation would lead to higher LTE column densities compared to the escape probability result and can thus not explain this discrepancy.

#### 4.1.3. Temperatures

We find a temperature gradient across the surface of the cloud, as traced by $^{12}$CO, from more than 70 K at the hot core position ($-90''$,$150''$) down to 20 K at the south-eastern edge of the mapped region. All three isotopomers are consistent with a single kinetic temperature of more than 20 K at position $(630'', -300'')$ and more than 30 K at $(0'', 0'')$.

At the other two positions, it is not possible to find a single temperature which is consistent with the emission of all three isotopomers: The parameters at $(270'', 60'')$ indicate a temperature gradient along the line of sight – from a warmer surface of more than 30 K, traced by the optical thick $^{12}$CO, to a colder interior with temperatures below 20 K, derived from $^{13}$CO and C$^{18}$O. Similarly, line ratios at the hot core position $(-90'', 150'')$ are not consistent with a constant kinetic temperature. In addition, a high temperature of at least 70 K is needed to explain the high $^{12}$CO 3–2/2–1 ratio of 1.5.

#### 4.1.4. Beam filling factors

Beam filling factors can now be determined by comparing the observed peak line temperatures with the expected values from the escape probablity analysis, given the kinetic temperatures, column and volume densities derived above ($F_b = T_{\rm mb}/T_{\rm model}$). In Table 5 we show the derived filling factors for the 2–1 transitions.

Filling factors $F_b$ range between 0.1 and 1.1, the values for $^{12}$CO and $^{13}$CO are consistently larger than those for C$^{18}$O. This may be due to the fact, that self shielding of C$^{18}$O is less effective than for the more abundant isotopomers, leading to photo destruction of C$^{18}$O at clump surfaces and thus a smaller emitting area within the beam.

**Table 5.** Beam filling factors $F_b$ derived from the observed $^{12}$CO 2–1 peak line temperature and the modelled temperature resulting from the escape probability analysis

| | (630,−300) | (270,60) | (0,0) | (−90,150) |
|---|---|---|---|---|
| $^{12}$CO 2–1 | 0.7 | 0.6 | 1.1 | 0.3 |
| $^{13}$CO 2–1 | 0.4 | 0.9 | 0.5 | 0.5 |
| C$^{18}$O 2–1 | – | 0.4 | 0.3 | 0.1 |

Secondly, the C$^{18}$O filling factors decrease systematically from positions inside the cloud, e.g. $(270'', 60'')$, to the cloud edge at $(-90'', 150'')$, falling from 0.4 to 0.1. This is consistent with an enhanced FUV field and photo destruction in the outer regions of Cepheus B near the HII region, relative to positions at greater distances to the HII region.

### *4.2. Volume filling factor*

For further description of the density structure in Cepheus B we compare the average density $n_{\rm av}$ derived from the LTE analysis with local densities $n_{\rm loc}$ derived from line ratios using the escape probability model. The ratio of average over local densities, the volume filling factor, is about $F_{\rm V}$=4%. Taking into account a possible interclump medium with the density of $n_{\rm ic}$, the volume filling factor can be estimated, $F_{\rm V} = (n_{\rm av} - n_{\rm ic})/(n_{\rm loc} - n_{\rm ic})$ and becomes even lower: the assumption of $n_{\rm ic} = 500$ cm$^{-3}$ e.g. leads to $F_{\rm V}$ =2%. Volume filling factors typically derived from multi-transitions studies range between a few% and 20% (e.g. Stutzki 1993) and provide indirect evidence for small scale structure.

Another way of putting this argument is considering the ratio of column densities over volume densities, $N/n_{\rm loc}$, found via the escape probability analysis (Table 4). This ratio gives a clump diameter of $D_{cl} \sim 0.02$ pc ($6''$) on average, significantly below the spatial resolution of the observations of $80''$ or 0.42 pc. From the above analysis, we know that beam filling factors reach values as low as 0.1. Still, this means that about 20 clumps or more lie within one beam.

The high surface temperature $> 70$ K, we derive at the hot core, and the small clump diameters $D_{cl} \sim 0.02$ pc calculated from the N/n$_{loc}$ ratio are confirmed directly by recent $^{12}$CO 7–6 observations of Kramer et al. (in prep.) with the Heinrich Hertz telescope at $14''$ (0.05 pc) resolution. Spatial structure is found down to the resolution limit. In addition, the peak line temperature of $\sim 50$ K indicates kinetic temperatures of at least

**Table 6.** Summed FUV fluxes $\chi$ of all 6 stars penetrating the clumpy cloud and distance $r'$[pc] to the hot core.

| | (630,60) | (630,−300) | (270,60) | (0,0) | (−90,150) |
|---|---|---|---|---|---|
| $r'$ | 2.6 | 3.7 | 1.7 | 0.7 | 0 |
| $\chi$ | 35 | 4 | 60 | 440 | 5600 |

70 K. Optically thin emission or a beam filling factor of less than 1, would mean even higher local kinetic temperatures.

All this shows that only a small volume of the whole cloud is filled with molecular material in dense clumps. Such a strong clumping allows the FUV radiation of the HII region S155 and the hot core compact HII region to penetrate the cloud far more than it would be possible in a homogenous cloud.

### *4.3. The UV field*

The UV field of O and B stars heats the molecular gas via the photoelectric effect on dust grain surfaces and via FUV pumping of $H_2$ (e.g. Kaufman et al. 1999). Together with the cosmic rays, it is thus directly influencing the emission of CO lines which are one of the main coolants of the gas. The primary sources of UV radiation in the vicinity of the Cepheus B molecular cloud are the O7 star HD217086 and the B1 star HD217061 (Fig. 1, projected distances to the hot core 1.2 pc and 0.7 pc) which are members of the Cepheus OB3 association lying to the north and west of the cloud interface to the HII region S155, and the embedded B1 star in the hot core region. Three more B stars – also members of the OB3 association (see Fig. 3 in Felli et al. 1978, projected distances to the hot core 2.6 pc, 3.8 pc and 5.1 pc) – lie in north-eastern direction, and contribute weakly to the FUV field impinging on Cepheus B.

The far-UV luminosity $L$ between 91 nm and 300 nm wavelength (13.6 eV and 6 eV), responsible for heating the cloud, is derived assuming that the star is a black body at the effective temperature corresponding to its spectral type (Panagia 1973). In addition, we assume that the distance $R$ from the star to a position inside the cloud is given by the projected distance. Estimating the geometrical dilution as well as the blockage and scattering by molecular clumps inside the cloud, the average UV-flux $S$ of each star at different positions inside the cloud can be calculated via (see Stutzki et al. 1988):

$$S = L/(4\pi R^2) \cdot exp[-(F_{\rm V}/D_{cl})(R - R_0)],$$

where $F_{\rm V}$ is a typical clump volume filling factor of 0.02 and $D_{cl}$ the typical clump diameter of 0.02 pc. $R_0$ is the distance between the position inside the cloud and the cloud surface, in the direction of the exciting star. The typical scale length, $F_{\rm V}/D_{cl}$, of the UV penetration is thus 1 pc.

Table 6 shows the derived fluxes $\chi$, as the sum of the fluxes of all 6 stars, in units of the average interstellar radiation field, $G_0 = 1.6 \times 10^{-3}$ erg s$^{-1}$ cm$^{-3}$ (Habing 1968). The FUV flux drops by three orders of magnitude, between the immediate interface region at the hot core, where fluxes rise to $\sim 6 \cdot 10^4$, and the south-eastern outskirts of the mapped region which are weakly illuminated by fluxes only slightly above the average interstellar field.

The position $(630'', 60'')$ represents the north-eastern edge of Cepheus B, where the line ratios of $^{12}$CO 3–2/2–1 rise again (Fig. 4) – maybe due to heating by three B stars which contribute a flux of 35.

### *4.4. PDR modelling of CO lines*

The above discussion shows that a homogeneous cloud model cannot consistently describe the observed line ratios of all three CO isotopomers at all positions, although such a model still provides first estimates on column densities, densities, clump sizes, and temperature gradients. Apparently contradictory line ratios appear to be a widespread phenomenon in photon illuminated clouds. Castets et al. (1990) interpreted similar findings in Orion A by temperature gradients increasing towards the cloud surfaces. Such gradients are naturally expected for UV irradiated clouds. Gierens et al. (1992) modelled the line ratios found in Orion A using a spherical symmetric PDR code including analytic temperature and density gradients. Störzer et al. (2000) present a more realistic cloud model which provides a self-consistent treatment of the chemical and thermal balance of a cloud together with the radiative transfer of CO line emission in spherical clouds illuminated by an isotropic FUV field. The model assumes the density to increase radially inward following a power law. Main input parameters determining the model are the average $H_2$ volume density, the average $H_2$ column density and the intensity of the FUV field. The clump diameter of the model is proportional to the ratio of column density over volume density, the thermal and chemical structure of the clump models are iteratively calculated from the balance of heating and cooling. However, this PDR model does not take into account the effects of several small clouds of varying sizes and masses within a single telescope beam nor internal heating sources. We thus expect the model to consistently describe most line intensities and ratios observed in Cepheus B, but not all details, thus refining our first analysis.

We compared the 4 measured peak line ratios, $^{12}$CO 3–2/2–1, $^{13}$CO 3–2/2–1, $^{12}$CO/$^{13}$CO 2–1, $^{12}$CO/C$^{18}$O 2–1 (Table 3), and the observed $^{12}$CO 2–1 line temperature (Fig. 3) with the model calculations, assuming an impinging FUV field of $\chi = 10^3$ (cf. Table 6). Note that the analysis of Störzer et al. (2000) indicates that the magnitude of the impinging FUV field does not lead to large variations of line ratios. We take into account a 20% error on the line ratios. This analysis was not done for position $(630'', -300'')$, because we did not measure all ratios there.

#### 4.4.1. Position $(0'', 0'')$

This position exhibits the strongest emission in $^{12}$CO 2–1 within the mapped region. The $^{12}$CO and $^{13}$CO 3–2/2–1 line ratios of 0.8 (Table 3) are – within the errobars – in the range of the expected ratios for thermalized emission in the LTE case and allow to derive the local $H_2$ density. The PDR model indicates densi-

ties of less than $3.2 \cdot 10^4\,\mathrm{cm}^{-3}$. Low $H_2$ column densities are indicated by the rather high inter-isotopic line ratios $^{12}$CO/C$^{18}$O and $^{12}$CO/$^{13}$CO 2–1 of 32 and 3.4 (Table 3). The PDR model predicts $H_2$ column densities per clump of $\leq 5 \cdot 10^{21}\mathrm{cm}^{-2}$ corresponding to an optical extinction $A_V$ of $\leq 5$ mag. Both, the upper limits on $n$ and $N$, are consistent to within a factor of 2 with the homogeneous cloud model (Table 4), which also leads to a consistent description.

The PDR model fails however to reproduce the observed $^{12}$CO peak line temperature of 26 K, it merely predicts line temperatures of $\leq 5$ K. At least 5, small overlapping clumps within the beam may reproduce the observed intensity since the optical depths are not high for the low column densities found at this position. Small clumps show the observed high $^{12}$CO/C$^{18}$O ratios due to two effects: photo-dissociation of C$^{18}$O in the surface regions leading to a smaller C$^{18}$O emitting region and lower kinetic temperatures in the clump interiors (cf. Zielinsky et al. 2000).

The next two positions are of particular interest, since the escape probability model does not allow to describe consistently all observed line ratios found at these positions.

#### 4.4.2. Position $(270'', 60'')$

With increasing distance to the HII region, the C$^{18}$O line temperatures rise and peak with 2.3 K at (270″,60″), at a distance of 1.7 pc to the hot core, indicating the position of highest column density. Also, in contrast to position (0,0), the $^{12}$CO 3–2/2–1 ratio differs significantly from the corresponding $^{13}$CO ratio indicating that both isotopomers trace different physical regions of the cloud. Indeed, the escape probability analysis (Table 4) indicates that the $^{12}$CO emission arises in (surface) regions of at least 30 K kinetic temperature while the $^{13}$CO emission stems from colder (interior) regions. Since the PDR model takes into account a temperature gradient, it allows to model consistently the data at this position and clearly improves on the esc.prob. models. The best fit to the PDR model is obtained for densities of about $6 \cdot 10^4\,\mathrm{cm}^{-3}$ and $H_2$ column densities of about $1.6 \cdot 10^{22}\,\mathrm{cm}^{-2}$. For these parameters, the model calculates a peak $^{12}$CO 2–1 line intensity of 14 K, exactly what is observed, indicating a beam filling factor of unity for this line.

#### 4.4.3. Position $(-90'', 150'')$

This position lies in the immediate vicinity of the hot core. Its influence is evident in the high $^{12}$CO 3–2 peak temperatures of 23 K (Table 3). However, C$^{18}$O intensities are low at this position. The $^{13}$CO 3–2/2–1, $^{12}$CO/$^{13}$CO 2–1, and $^{12}$CO/C$^{18}$O 2–1 peak line temperature ratios (Table 3) are similar to the ratios found at position $(0'', 0'')$. The PDR model leads to $H_2$ densities of less than $6.3 \cdot 10^4\,\mathrm{cm}^{-3}$ and $H_2$ column densities of less than $4.5 \cdot 10^{21}\,\mathrm{cm}^{-2}$. The observed $^{12}$CO 2–1 line peak temperature is 16 K, the model gives $\leq 5$ K, indicating again that several small clumps lie within the beam, and their added emission produces the observed higher line temperatures.

**Table 7.** Results of the PDR analysis derived from four peak line ratios and $^{12}$CO 2–1 peak line intensities. Remarks: (1) The analysis at position $(-90'', 150'')$ ignores the high $^{12}$CO 3–2/2–1 ratio which cannot be reproduced. (2) Clump diameters are derived from the upper limits found for $N$ and $n$.

| | (270,60) | (0,0) | $(-90,150)^{(1)}$ |
|---|---|---|---|
| $N(\mathrm{H_2})[10^{22}\mathrm{cm}^{-2}]$ | $\approx 1.6$ | $\leq 0.5$ | $\leq 0.45$ |
| $n_{\mathrm{loc}}(\mathrm{H_2})[10^4\mathrm{cm}^{-3}]$ | $\approx 6$ | $\leq 3.2$ | $\leq 6.3$ |
| $N/n_{\mathrm{loc}}^{(2)}$[pc] | 0.09 | $\approx 0.5$ | 0.002 |
| $F_b$ | $\approx 1$ | $\geq 5$ | $\geq 3$ |

However, in contrast to position $(0'', 0'')$, the large $^{12}$CO 3–2/2–1 ratio of 1.5 cannot be reproduced by the same model clump, neither can it be reproduced by any of the models presented by Störzer et al. (2000). In these models, calculated ratios rise to about 1.1 for very high volume densities of $n > 10^6\,\mathrm{cm}^{-3}$ and low column densities of $N < 2.5\,10^{21}\,\mathrm{cm}^{-2}$, which are the lowest column density analyzed by Störzer et al.. Column densities lower than that would render the $^{12}$CO lines optically thin. In this limit ratios of 1.5 could be explainable by excitation temperatures of more than 40 K.

### *4.5. Atomic carbon*

Additionally, we observed the $^3\mathrm{P}_1 \rightarrow {}^3\mathrm{P}_0$ transition of atomic carbon at two positions, at (0″/0″) position and at $(-150''/150'')$, near the edge to the HII region S155. Fig. 6 presents the [CI] spectra in comparison with $^{13}$CO spectra. The line shapes look similar in the wings, but the core emission of CI is less intense than in $^{13}$CO, maybe a signature of CI self-absorption. Table 8 presents line parameters and ratios between the three transitions. The $^{13}$CO and [CI] ratio of integrated intensities $\int T_{\mathrm{mb}} dv$ do not vary significantly between the two positions. Regarding (0″/0″) as representative for the bulk of the cloud and $(-150''/150'')$ as representative for the cloud edges, this may suggest a similar spatial distribution for CI compared with $^{13}$CO.

With the CI data, the abundance ratio of molecular to atomic carbon can be estimated. Assuming optically thin [CI] emission and LTE allows to derive a lower limit of the CI column density (Frerking et al. 1989):

$$N(\mathrm{CI}) = 5.94 \cdot 10^{15} \frac{1 + 3e^{\frac{-23.6}{T_{ex}}} + 5e^{\frac{-62.4}{T_{ex}}}}{3e^{\frac{-23.6}{T_{ex}}}} \int T_{\mathrm{mb}} dv \,[\mathrm{cm}^{-2}]$$

with $T_{\mathrm{ex}}$ taken from the $^{12}$CO 3–2 transition.

To compare gas phase abundances of carbon relative to CO we calculate LTE column densities for CO by multiplying $^{13}$CO (optically thin) column densities with the abundance factor of 67 (Table 9). At the two positions observed we find that the abundance of atomic carbon is 17% and 30% of the CO column densities. As expected the CI/CO ratio is rising at the cloud edges, because more molecular material is dissociated there due to the impinging FUV field. This phenomenon is also confirmed by the decreasing FWHM ratio of CO to atomic carbon. Because

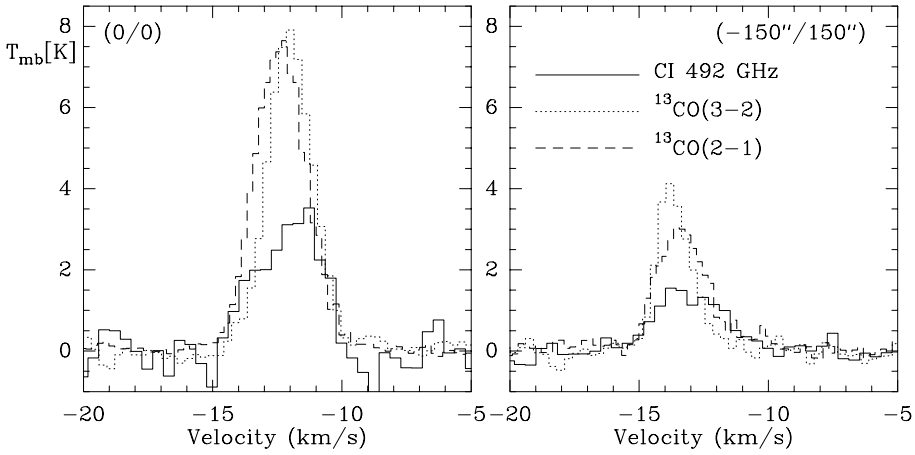


**Fig. 6.** Spectra of CI (492 GHz) and $^{13}$CO at two positions in Cepheus B

**Table 8.** Parameters of the CI and $^{13}$CO spectra: peak temperatures, integrated intensities and FWHM

| | $T_{\rm mb}[K]$ | $\int T_{\rm mb} dv$ [K km s$^{-1}$] | FWHM [km s$^{-1}$] |
|---|---|---|---|
| $(0''/0'')$ | | | |
| CI 492 GHz | 3.4 | 12.0 | 2.7 |
| $^{13}$CO 3–2 | 7.8 | 17.0 | 2.0 |
| $^{13}$CO 2–1 | 7.5 | 19.0 | 2.4 |
| $^{13}$CO 3-2/CI | 2.3 | 1.4 | 0.7 |
| $^{13}$CO 2-1/CI | 2.2 | 1.6 | 0.9 |
| $(-150''/150'')$ | | | |
| CI 492 GHz | 1.5 | 4.9 | 3.1 |
| $^{13}$CO 3–2 | 4.0 | 6.6 | 1.6 |
| $^{13}$CO 2–1 | 3.0 | 7.2 | 2.3 |
| $^{13}$CO 3–2/CI | 2.7 | 1.4 | 0.5 |
| $^{13}$CO 2–1/CI | 2.0 | 1.5 | 0.7 |

**Table 9.** CI and $^{12}$CO column densities

| | $(0''/0'')$ $T_{\rm ex} = 34$K | $(-150''/150'')$ $T_{\rm ex} = 29$ K |
|---|---|---|
| $N$(CI) [cm$^{-2}$] | $1.5 \cdot 10^{17}$ | $0.8 \cdot 10^{17}$ |
| $N$(CO) [cm$^{-2}$] | $8.7 \cdot 10^{17}$ | $2.7 \cdot 10^{17}$ |
| $N$(CI)/$N$(CO) | 0.17 | 0.3 |

of the unknown CI opcacity these abundance ratios are only lower limits. Tauber et al. (1995) derived 0.17 as lower limits for the Orion bar, and Plume et al. (1999) find values between 0.32 and 0.47 for a sample of clouds.

## 5. Discussion

In Table 10 we compare the line ratios found in Cepheus B with those found in two other galactic star forming regions: M17 (Wilson et al. 1999, cf. Table 5 therein) and Orion B (Kramer et al. 1996). Like the Cepheus B observations presented here, both data sets stem from large scale observations covering not only the immediate vicinity of sites where star formation is taking place but also the distant quiescent parts of the clouds far from the cloud interfaces with HII regions. While the FUV fields do not exceed a few $10^3$ in Cepheus B, they are stronger by at least a factor of 10 in the NGC 2024 region within Orion B and still stronger in the interface region of M17SW (Genzel et al. 1989).

Local volume densities of $\sim 10^5$ cm$^{-3}$ are needed to explain the observed average line ratios found in Orion B (Kramer et al. 1996), while densities of $\sim 10^4$ are sufficient in the case of Cepheus B at all positions, due to the lower 3–2/2–1 line ratios. The average line ratios found in M17 are consistent with densities of $10^4$ or more (Fig. 6 in Wilson et al. 1999).

The variation of the $^{12}$CO 3–2/2–1 integrated intensity ratio along different lines of sight is stronger in Cepheus B and Orion B than in the M17 observations of Wilson et al.. The ratio rises significantly above 1 near the hot core and at the north-eastern edge in Cepheus B, and in the NGC 2024/IC434 interface region of Orion B. Small clumps with densities of more than $10^6$ may explain the ratio of 1.3 found in the latter region. However, higher ratios, like those found in parts of Cepheus B cannot easily be explained. Models taking into account internal heating sources and/or heating by shocks may be necessary.

For all three clouds, the $^{12}$CO/$^{13}$CO 3–2 and 2–1 ratios vary much stronger than the interisotopomeric ratios (see Fig. 5), indicating that variations of column densities dominate while the local densities traced by $^{12}$CO line ratios are more or less constant. In addition, $^{12}$CO/$^{13}$CO integrated intensity ratios in general rise towards the edges of all three clouds, where the integrated intensities drop and $^{13}$CO is becoming optical thin.

Our results confirm the findings of other authors (e.g. Plume et al. 1999, Minchin & White 1995, White & Sandell 1995) who reported rising $^{13}$CO/C$^{18}$O line ratio with dropping column density at the cloud edges, from a typical galactic value of $\sim 5$ at the position of highest column density to values of 50 and higher at low column densities. At the edges of molecular clouds, where optical extinction is low, $^{13}$CO is expected to be enriched in comparison with C$^{18}$O due to isotope-selective photodissociation and/or chemical fractionation (see e.g. the PDR models of Sternberg & Dalgarno 1989). It is thus tempting to interpret the observations as a confirmation of the isotopomeric fractionation predicted by PDR models.

**Table 10.** Comparison of line ratios of integrated intensities with observations of M17 and Orion B (Cepheus B: this paper; M17: Wilson et al. 1999, Tables 2–4 therein; Orion B: Kramer et al. 1996)

| | average ratios | | | range of ratios | | |
|---|---|---|---|---|---|---|
| | Cepheus B | M17 | Orion B | Cepheus B | M17 | Orion B |
| $^{12}$CO 3–2/2–1 | 0.8 | 0.8 | 1 | 0.7–3 | 0.63–0.83 | 0.7–1.3 |
| $^{13}$CO 3–2/2–1 | 0.5 | 1.3 | 1 | 0.3–0.9 | 0.78–1.45 | – |
| $^{12}$CO/$^{13}$CO 2–1 | 3.8 | 4.5 | 6 | 2–40 | 1.5–21 | 1.5–11 |
| $^{12}$CO/$^{13}$CO 3–2 | 6.9 | 3.7 | 6 | 2–20 | 1.4–8 | – |

Zielinsky et al. (2000), however, show that this straightforward conclusion is misleading, because the line-of-sight column density traced by the rare isotopomeric CO lines and the UV extinction column density responsible for the selective photoshielding and -destruction are not necessarily correlated, in particular in the edge-on geometries commonly observed. They explain the observed correlation as a natural consequence of a clumpy cloud PDR model. In small clumps (resulting in low column densities), self shielding of $^{13}$CO is much more effective than that of C$^{18}$O, the latter is nearly totally photodissociated which leads to high $^{13}$CO/C$^{18}$O line ratios. On the other hand, in large clumps (resulting in high column densities) even C$^{18}$O is protected to a large degree from photodissociation and the $^{13}$CO/C$^{18}$O ratios decrease.

## 6. Summary

Investigating the global properties of the sequential star forming region Cepheus B, we mapped the molecular cloud in 6 lower-$J$ transitions of CO and its isotopomers. Multi line analysis with two radiative transfer codes were conducted and revealed the following results:

- We find a temperature gradient perpendicular to the line of sight from around 70 K near the HII region down to 20 K at the south-eastern end of the mapped region.
- At the column density peak position – at 1.7 pc distance to the hot core – the data are consistent with a decreasing temperature gradient along the line of sight.
- These temperature gradients imply that the whole cloud is still in a relatively calm state. Star formation takes place just around the hot core, maybe triggering further star formation deeper inside Cepheus B in the future.
- The exciting FUV flux is supplied mostly by an O7 and a B1 star in the west with little contributions from other members of the OB association in the north-east. The flux varies between $\approx 5 \times 10^3$ near the HII region and around a few at the south-eastern edge of the mapped region (in units of the average interstellar radiation field).
- Local $H_2$ densities are about $2 \cdot 10^4$ cm$^{-3}$ while the average $H_2$ density is less than $10^3$ cm$^{-3}$, thus, volume filling factors range between 2% and 4%, and the average clump diameter is estimated to be 0.02 pc.
- CI observations indicate lower limits for the abundance ratio of atomic to molecular carbon between 0.15 and 0.3.
- $^{12}$CO/$^{13}$CO ratios are well correlated with the corresponding integrated $^{13}$CO intensities, most likely this is due to optical depths effects.
- $^{13}$CO/C$^{18}$O ratios rise at the cloud edges. Recent investigations by Zielinsky et al. (2000) reveal that a clumpy cloud PDR model is capable to naturally explain the observed line ratios.
- The homogenous Escape Probability model is only partly able to reproduce the observed data set, while the more sophisticated PDR model, with only the average density and the clump radius as free parameters, of Störzer et al. (2000) reproduces most observed line ratios. An exception is the high $^{12}$CO ratio at the hot core position. Probably, models which include inner heating sources are capable to explain such ratios in the future.

*Acknowledgements.* The KOSMA 3m submillimeter telescope at the Gornergrat-Süd is operated by the University of Cologne in collaboration with Bonn University, and supported by special funding from the Land NRW. The observatory is administered by the International Foundation Gornergrat & Jungfraujoch.

## Appendix A: on-the-fly observing mode

Scanning a radio source at a constant speed while continuously integrating the received data over certain time intervals, such that a grid of data results, is the essence of the OTF observing mode. The lack of dead times between the different ON positions and less time on the OFF position makes this mode much more effective than the raster mapping mode where, for data integration, the telescope stops at each ON position. However, collecting data "on-the-fly" causes a "smearing", i.e. broadening, of the effective beam along the scanning direction.

### *A.1. Beam smearing and sampling*

In order to quantify the "smearing" effect we neglect, for the sake of simplicity, the fact that the beam has a two-dimensional structure and consider only its one-dimensional profile along the scanning direction.

Let $\Theta$ be the respective coordinate in the plane of the sky, $\Delta\Theta$ the width of each of the integration intervals, and $b(\Theta)$ the intrinsic beam pattern. The (normalized) effective OTF beam pattern, $b_{\rm OTF}$, is then given by the convolution of the original

beam pattern and the box function, i.e.

$$b_{\rm OTF}(\Theta) \;=\; \frac{1}{b_0}\int_{-\infty}^{\infty} b(\Theta')\sqcap(\Theta-\Theta',\Delta\Theta)\,{\rm d}\Theta'\,, \qquad \text{(A.1)}$$

where the box function, $\sqcap(\Theta,\Delta\Theta)$, is defined by

$$\sqcap(\Theta,\Delta\Theta) = \begin{cases} 1/\Delta\Theta & \text{for} \quad -\Delta\Theta/2 \le \Theta \le \Delta\Theta/2 \\ 0 & \text{else} \quad . \end{cases} \qquad \text{(A.2)}$$

and where

$$b_0 = \int_{-\infty}^{\infty} b(\Theta')\sqcap(\Theta',\Delta\Theta)\,{\rm d}\Theta'\,. \qquad \text{(A.3)}$$

The normalization is such that $b_{\rm OTF}(0)=1$.

### A.11. Critical sampling

As shown by antenna theory, the Fourier transform of the telescope beam $\hat{b}(x)$ vanishes at the well-known cutoff frequency $x_c = D/\lambda$, where $D$ and $\lambda$ denote the diameter of the antenna and the observing wavelength respectively. Hence,

$$\hat{b}_{\rm OTF}(x) = \hat{b}(x)\,\frac{\sin(\pi x\Delta\Theta)}{\pi x\Delta\Theta}\,, \qquad \text{(A.4)}$$

vanishes at $x_c$ as well, implying that $b_{\rm OTF}(\Theta)$ is a band limited function that, according to the Nyquist theorem, is fully specified by values spaced at equal intervals not exceeding $\Delta\Theta_c = 1/(2x_c) = \lambda/(2D)$. In Eq. (A.4), the effect of the OTF mode enters only via the sinc function which does not affect $x_c$. Adopting $\Delta\Theta = \Delta\Theta_c$ the first zero of the sinc function is at $x' = (2D)/\lambda$ which is already beyond the critical frequency. OTF broadening of the effective beam may be regarded as a slightly enhanced edge taper along the scanning direction. One should also note that disturbing effects due to an imperfect surface of the dish, aperture blocking by the secondary and the feed legs, or spillover at the edges of the primary and secondary, while causing changes in the details of the frequency distribution $\hat{b}(x)$, do not affect the cutoff frequency. This is also true taking the two-dimensional structure of the beam into account. Thus we conclude that, from a rigorous point of view, critical Nyquist sampling provides the maximum spatial information both in the position switching modes and the OTF mode.

Usually, the Nyquist interval is expressed in units of the HPBW of the antenna. With an edge taper of $-14$dB, the HPBW $\approx 1.2\lambda/D$ (e.g. Goldsmith 1982), and $\Delta\Theta_c \approx$ HPBW/2.4.

### A.12. Effective beam width

Employing (A.1) and (A.3), the effective width of the OTF beam, $\Omega_{\rm OTF}$, corresponding to the "beam solid angle" of a real antenna, reads

$$\Omega_{\rm OTF} \;=\; \int_{-\infty}^{\infty} b_{\rm OTF}(\Theta)\,{\rm d}\Theta = \frac{\Omega}{b_0}\,, \qquad \text{(A.5)}$$

where $\Omega = \int b\,{\rm d}\Theta$ denotes the effective width of the original beam. Approximating the original beam by a simple Gaussian, i.e. $b(\Theta) = \exp(-4\ln 2\,\Theta^2/{\rm HPBW}^2)$, and putting $\Delta\Theta = \Delta\Theta_c =$ HPBW/2.4, one finds a ratio of the effective widths of

$$\frac{\Omega_{\rm OTF}}{\Omega} = \frac{1}{b_0} = 1.04\,. \qquad \text{(A.6)}$$

Thus, for integration intervals not exceeding the critical Nyquist sampling intervals, the on-the-fly observing mode leads to an effective broadening of the beam along the scanning direction of at most four percent. One finds an even slightly smaller amount, taking the two-dimensional structure of the beam into account.

We therefore decided to sample the Cepheus B cloud at approximately the Nyquist interval at 345 GHz, i.e. $30''$, in scanning direction as well as perpendicular to it.

## Appendix B: error beam correction

The KOSMA main beam efficiency at 345 and 330 GHz was only 55% in October 98. The telescope beam therefore detected a substantial fraction of the power with underlying error beam(s) caused by surface deviations of the telescope primary mirror from the ideal paraboloid. Imperfections are mainly caused by misalignment of the 18 primary panels, since the individual panels are nearly perfect ($\sim 5\,\mu$m rms). Following the argument of Greve et al. (2000, Eq. 12) who discuss the error beams of the IRAM 30m telescope, the KOSMA telescope probably had an error beam with a width of $0.53\,\lambda/(L/2)$ with the observing wavelength $\lambda$ and the correlation length $L$ of surface deformations. The correlation length is roughly given by the mean panel diameter, i.e. $\sim 63$ cm. The estimated error beam width thus is $302''$. We rely on this estimate, since direct measurements, derived e.g. from observations of the moon edge, are missing.

Using the main beam efficiency to derive the source brightness temperature distribution leads to temperatures which are too high when extended objects are observed. In addition, the underlying error beam leads to a smearing of the intensity distribution. We corrected for the error beam using the second-order deconvolution method applied by Westerhout et al. (1973) to 21 cm data of the NRAO 300 ft radio telescope. See Bensch et al. (2000) for a discussion of other possible correction methods. The corrected brightness temperature averaged over the main beam is given by

$$T_{\rm mb,c} = \overline{T} = \frac{F_{\rm eff}}{B_{\rm eff}}\,T_A^* - \frac{\Omega_{300}}{\Omega_{\rm mb}}\overline{T_{300}}, \qquad \text{(B.1)}$$

$$\text{with}\;\; \frac{F_{\rm eff}}{B_{\rm eff}} = \frac{1}{\eta_B} = \frac{\Omega_{2\pi}}{\Omega_{\rm mb}}$$

where $\Omega_{2\pi}$, $\Omega_{300}$, $\Omega_{\rm mb}$ are the integral of the beam pattern over the forward hemisphere, error beam, and main beam of the telescope. $\overline{T_{300}}$ is the brightness temperature averaged over the error beam. $\overline{T_{300}}$ can be expressed in terms of $T_A^*$, analogous to Westerhout et al. (1973, Eq. 10), but for only one error beam:

$$T_{\rm mb,c} = \frac{F_{\rm eff}}{B_{\rm eff}}\Big(T_A^* - \frac{\Omega_{300}}{\Omega_{\rm mb}}F_{300}\star T_A^* + \qquad \text{(B.2)}$$

$$\frac{\Omega_{300}^2}{\Omega_{\rm mb}(\Omega_{\rm mb}+\Omega_{300})}F_{300}\star F_{300}\star T_A^*\Big)$$

where $F_{300} \star T_A^*$ is the original data convolved with a Gaussian of $300''$ width, the width of the error beam. With $F_{\rm eff} = 0.9$, $B_{\rm eff} = 0.55$, $\Omega_{300}/\Omega_{\rm mb} = (F_{\rm eff} - B_{\rm eff})/0.55 = 0.64$, and $F_{300} \star F_{300} = F_{425}$, we obtain:

$$T_{\rm mb,c} = 1.64\Big(T_A^* - 0.64 F_{300} \star T_A^* + 0.25 F_{425} \star T_A^*\Big) \quad \text{(B.3)}$$

or $T_{\rm mb,c} = 1.64\,(T_A^* - E)$ where $E$ is the error beam contribution. Note that this is not only a simple scaling factor to the spectra. Instead, the varying errorbeam pickup is corrected for both in position and velocity, thus also possibly correcting line profiles. Resulting maps show an enhanced contrast (Figs. 1,2).

The region mapped at 345 GHz is $1050'' \times 840''$, a factor of 10 larger than the error beam. We therefore anticipate the correction to work in the interior parts of the map including all four positions selected for a detailed analysis, but not at the map edges.

## References


Bensch F., Panis J.-F., Stutzki J., Heithausen A., Falgarone E., 2000, A&A, in press

Blaauw A., 1964, ARA&A, 213

Castets A., Duvert G., Bally J., Langer W., Wilson R., 1990, A&A 234, 469

Cesaroni R., Felli M., Walmsley M., 1999, A&AS 136, 333

Downes D., 1989, In: Appenzeller I.,Habing H.J., Léna P. (eds.) Evolution of Galaxies, Astronomical Observations. Springer Verlag, Heidelberg

Felli M., Tofani G., Harten R., Panagia N., 1978, A&A 69, 199

Flower D., Launay J., 1985, MNRAS 214, 271

Frerking M., Langer W., Wilson R., 1982, ApJ 262, 590

Frerking M., Keene J., Blake G., Philipps T., 1989, ApJ 344, 311

Genzel R., Harris A., Stutzki J., 1989, Proceedings of the 22nd Eslab Symposium on Intrared Spectroscopy in Astronomy, Salamanca, Dec. 7–9 1988 (EeSA SP series)

Gierens K., Stutzki J., Winnewisser G., 1992, A&A 259, 271

Goldsmith, P.F., 1982, In: Button K.J. (ed.) Infrared and Millimeter Waves. Vol.6: Systems and Components. Academic Press, New York, p. 277

Graf U., Haas S., Honingh C., et al., 1998, In: Phillips T.G. (ed.) SPIE, International Symposium on Astronomical Telescopes and Instrumentation, Kona, Hawaii, USA

Greve A., Kramer C., Wild W., 1998, A&AS 133, 271

Griffin M.J., Ade P.A.R., Orton G.S., et al., 1986, Icarus 65, 244

Grossman E., 1989, AT-Atmospheric Transmission Software. User's Manual. Univ. of Texas, Austin

Haas S., Honingh, C.E., Hottgenroth D., Jacobs K., Stutzki J., 1997, Int. J. on Infrared and Millimeter Waves 493, 17

Habing, H.J., 1968, Bull. Astr. Inst. Netherlands 19, 421

Hughes V.A., 1988, ApJ 333, 788

Kaufman M., Wolfire M., Hollenbach D., Luhman M., 1999, ApJ 527, 795

Kramer C., Stutzki J., Winnewisser G., 1996, A&A 307, 915

Kramer C., Degiacomi C.G., Graf U.U., et al., 1998, In: Phillips T.G. (ed.) SPIE, International Symposium on Astronomical Telescopes and Instrumentation, Kona, Hawaii, USA

Kramer C., Beuther H., Simon R., Stutzki J., Winnewisser G., 2000, In: Mangum J.G. (ed.) PASP, Imaging at Radio through Submillimeter Wavelengths. Tucson, USA

Langer W., Penzias A., 1990, ApJ 357, 477

Lovas F., 1988, J. Phys. Chem. Ref. Data, Vol. 15, No. 1, 251

Miller J., 1968, ApJ 78, 929

Minchin N., Ward-Thomson D., White G., 1992, A&A 265, 733

Minchin N., White G., 1995, A&A 302, L25

Moreno-Corral M., Chavarria-K.C., Lara E., Wagner S., 1993, A&A 98, 295

Olmi L., Felli M., 1998, A&A 339, 872

Panagia N., 1973, ApJ 78, 929

Plume R., Jaffe T., Tatematsu K., Evans N., Keene J., 1999, ApJ 512, 768

Sargent A., 1977, ApJ 218, 736

Schieder R., Tolls V., Winnewisser G., 1989, Exp. Astron. 1, 101

Schröder K., Staemmler V., Smith M., Flower D., Jacquet R., 1991, J. Phys. B 24, 2487

Sternberg A., Dalagarno A., 1989, ApJ 338, 197

Störzer H., Zielinsky M., Stutzki J., Sternberg A., 2000, A&A 358, 682

Stutzki J., Winnewisser G., 1985, A&A 144, 13

Stutzki J., Stacey G.J., Genzel R., et al., 1988, ApJ 332, 379

Stutzki J., 1993, Rev. Mex. Astron. Astrofis. 6, 209

Stutzki J., Graf U.U., Haas S., et al., 1997, ApJ 477, L33

Tauber J., Lis D., Keene J., Schilke P., Büttgenbach T., 1995, A&A 297, 567

Testi L., Olmi L., Hunt L., et al., 1995, A&A 303, 881

Westerhout G., Wendlandt H.U., Harten R.H., 1973, AJ 78, 569

White G., Sandell G., 1995, A&A 299, 179

Wilson C.D., Howe J.E., Balogh M.L., 1999, ApJ 517, 174

Winnewisser G., Bester M., Ewald R., et al., 1986, A&A 167, 207

Winnewisser G., Zimmermann P., Hernichel J., et al., 1990, A&A 30, 248

Zielinsky M., Stutzki J., Störzer H., 2000, A&A 358, 723